Blanching Defects at Pressure Points: Observations from Dynamic Total-Body PET/CT Studies

Yasser G. Abdelhafez[1,2], Kristin McBride[1], Edwin K. Leung[1,3,4], Heather Hunt[1], Benjamin A. Spencer[1], Javier E. Lopez[5,6], Kwame Atsina[5,6], Elizabeth J. Li[3], Guobao Wang[1], Simon R. Cherry[1,3], Ramsey D. Badawi[1,3], Fatma Sen[1], and Lorenzo Nardo[1]

[1]Department of Radiology, University of California, Davis, California; [2]Nuclear Medicine Unit, South Egypt Cancer Institute, Assiut University, Assiut, Egypt; [3]Biomedical Engineering, University of California, Davis, California; [4]UIH America, Inc., Houston, Texas; [5]Department of Internal Medicine, University of California, Davis, California; and [6]Cardiovascular Research Institute, University of California, Davis, California

Total-body PET/CT allows simultaneous acquisition of all body parts at a single bed position during the radiotracer uptake phase. Dynamic imaging protocols using total-body PET might demonstrate findings that may not have been previously visualized or described using conventional PET/CT scanners. We examined the characteristics of blanching defects—areas of markedly reduced (partial defect) or absent (complete defect) radiotracer uptake seen at the skin and subcutaneous tissues opposite the bony prominences at pressure points. **Methods:** In this observational study, 77 participants underwent dynamic total-body PET/CT imaging using ^{18}F-FDG (group 1, $n = 47$, 60-min dynamic, arms down, divided into 3 subgroups according to the injected dose) or ^{18}F-fluciclovine (group 2, $n = 30$, 25-min dynamic, arms up). Forty of the 47 participants in group 1 were reimaged at 90 min after being allowed off the scanning table. Blanching defects, partial or complete, were characterized opposite the bony prominences at 7 pressure points (the skull, scapula, and calcaneus bilaterally, as well as the sacrum). The association of the blanching defects with different clinical and technical characteristics was analyzed using uni- and multivariate analyses. **Results:** In total, 124 blanching defects were seen in 68 of the 77 (88%) participants at one or more pressure points. Blanching defects were higher, on average, in group 2 (3.5 ± 1.7) than in group 1 (2.1 ± 1.4; $P < 0.001$) but did not vary within group 1 for different ^{18}F-FDG dose subgroups. All defects resumed a normal pattern on delayed static (90-min) images, except for 14 partial defects. No complete blanching defects were seen on the 90-min images. By multivariate analysis, arm positioning above the head was associated with skull defects; scapular and sacral defects were significantly more common in men and in those with a lower body mass index, whereas calcaneal defects were not associated with any factor. **Conclusion:** Blanching defects opposite the bony pressure points are common on dynamic total-body PET/CT images using different radiopharmaceuticals and injection doses. Their appearance should not be immediately interpreted as an abnormality. The current findings warrant further exploration in a prospective setting and may be used to study various mechanopathologic conditions, such as pressure ulcers.

Key Words: total-body PET/CT; dynamic scans; pressure points; blanching defects; skin and subcutaneous tissue

Received Jan. 24, 2022; revision accepted Mar. 22, 2022.

For correspondence or reprints, contact Yasser G. Abdelhafez (yabdelhafez@ucdavis.edu).

Published online Apr. 19, 2022.

J Nucl Med Technol 2022; 50:327–334
DOI: 10.2967/jnmt.122.263905

Total-body PET/CT has recently been implemented in both research and clinical fields (*1,2*). The uEXPLORER total-body PET/CT scanner's long axial field of view of 194 cm not only allows for simultaneous acquisition of radiotracer kinetics across the entire body but also improves signal collection efficiency, which, coupled with high spatial resolution, results in high-resolution and high-quality images (*3*). For the first time, it is now possible to obtain high-quality total-body dynamic images that can be used in both research and the clinic (*4*). In the research field, total-body dynamic imaging has been described and is useful for such purposes as obtaining biomarkers characterizing the delivery and uptake of ^{18}F-FDG (e.g., K_1 and inhibition constant) via kinetic modeling (*5–9*). In the clinical field, dynamic imaging has been suggested by different groups for a variety of applications. For example, in the imaging of prostate cancer, dynamic imaging helps tumor detection and characterization, especially in the pelvis (*10–12*). Several guidelines have incorporated dynamic acquisitions as part of their recommended imaging protocols (*13–17*). However, the implementation of high-resolution and high-quality total-body acquisitions may enhance the prominence of additional findings that have not been previously described in the literature.

In this work, we characterized, for the first time to our knowledge, the presence of markedly reduced or absent radiotracer uptake at the skin and subcutaneous tissues opposite the bony prominences at pressure points, described hereafter as blanching defects, which were noted on dynamic total-body PET images performed with ^{18}F-FDG or ^{18}F-fluciclovine.

MATERIALS AND METHODS

Study Participants

This was a retrospective review of 4 institutional review board–approved studies prospectively acquired for other research purposes (approvals 1341792, 1374902, 1470016, and 1480948).

All participants provided written informed consent before being scanned. The participants were categorized into 2 groups according to the injected tracer: group 1 (^{18}F-FDG) included 47 participants under 3 subgroups according to the injected radiotracer dose (Table 1), and group 2 (^{18}F-fluciclovine) included 30 men with prostate cancer who were referred for a standard-of-care evaluation using ^{18}F-fluciclovine total-body PET/CT.

Total-Body PET/CT Scanning

All participants underwent list-mode dynamic PET/CT as part of their respective study protocol, on a total-body PET/CT scanner (uEXPLORER; United Imaging Healthcare) (*3*). The scanner has an axial field of view of 194 cm, a PET spatial resolution of no more than 3.0 mm in full width at half maximum near the center of the axial field of view, and an 80-detector-row CT component with a minimum slice thickness of 0.5 mm. Before acquisition of the dynamic PET data, a low-dose (tube current, ~50 mA) or ultralow-dose (tube current, ~5 mA) CT scan (both with a tube voltage of 140 kVp) was acquired for attenuation correction and anatomic localization. The tube current was automatically modulated by the scanner manufacturer's algorithm.

All PET data were acquired in list-mode format with the participants supine. Positioning aids were provided according to the participant's comfort level. For group 1, all participants were positioned with arms down and underwent dynamic, 60-min acquisitions, starting at the time of intravenous injection of an ^{18}F-FDG dose ranging from 17.2 to 393.8 MBq (dose groups are summarized in Table 1). The last 20 min of acquisition (40–60 min after injection) were reconstructed into a single frame for the purpose of reviewing. According to their respective protocols, 40 of the 47 participants in group 1 were reimaged for 20 min starting at 90 min after injection (i.e., ~30 min after the end of the dynamic acquisition). Participants were allowed to get off the scanner table between scans and empty their urinary bladder. The second scan was used to assess changes within the blanching defects noted on the first set of images (the dynamic acquisition). Seven participants in group 1, all with cancer, underwent a follow-up dynamic scan after a median of 16 d (range, 14–24 d) for other research purposes. These follow-up scans were used to monitor the stability of the distribution of blanching defects.

For group 2, arms were positioned above the head in 29 of the 30 subjects and to the sides in a single subject. PET images were acquired for a total of 25 min, starting immediately after injection of 314.6 ± 19.7 MBq (range, 287.2–389.6 MBq) of ^{18}F-fluciclovine. The PET data were reconstructed into two 10-min frames (4–14 min and 15–25 min) for the purpose of reviewing.

All images were reconstructed using the vendor's software, which uses a time-of-flight, ordered-subset expectation maximization algorithm, with 4 iterations and 20 subsets. Attenuation-corrected and non–attenuation-corrected images were generated for analysis. All PET corrections were applied to the attenuation-corrected images (scatter, randoms, dead time, and normalization). No point-spread function modeling or postreconstruction smoothing was applied. The reconstruction matrix size was 256 × 256, generating 2.344-mm isotropic voxels. The described reconstruction parameters are the same as used for the routine clinical readouts (*1,2*).

PET/CT Image Analysis

The reconstructed PET/CT images were transferred to an image viewing workstation running OsiriX MD, version 12.0 (Pixmeo), and reviewed independently by 2 nuclear medicine physicians (5 and 13 y of PET/CT experience after training). Agreement between the 2 readers was considered the final reading. For discordant readings, a third nuclear medicine physician (20 y of experience) was consulted, masked to prior readings, and the final decision was based on the agreement of any 2 readers.

Both attenuation-corrected and non–attenuation-corrected images were reviewed side by side for any skin or subcutaneous areas of complete (grade 2) or partial (grade 1) absence of the expected normal radiotracer uptake (grade 0) compared with the surrounding tissues at different pressure points. Figure 1 illustrates examples of partial and complete defects. The pressure points were defined as the anatomic locations where a bony structure could restrict blood flow to the overlying tissues because of patient positioning or weight burden. For the current analysis, 4 locations, named after their bony prominences, were studied: skull, scapulae, sacrum, and calcaneus. Except for the sacrum, laterality was also noted as right, left, or bilateral. In the presence of bilateral defects with different defect grades, the higher grade was recorded for that pressure point.

For participants who underwent additional static scans at 90 min after injection, the images were read after recording the impression from the dynamic dataset.

PET/CT images were reviewed for any visual gross misregistration between PET and CT at the pressure points and for the presence of any anatomic abnormality in the studied pressure points (e.g., skin ulceration or masses). The CT window level was adjusted to identify and precisely locate the different positioning aids (e.g., back or knee cushions) on the CT images (Fig. 1).

Statistical Analysis

Differences in continuous data (e.g., age and body mass index [BMI]) were compared between the 2 primary groups (with and without blanching defects) using the independent-samples t test for normally distributed data and the Mann–Whitney U test for nonnormally distributed data. Differences in qualitative features were compared using the χ^2 test or the Fisher exact test, as appropriate. Both participant- and site-based analyses were performed. A participant with a blanching defect at one or more sites was considered positive for blanching defects. Individual factors that showed some association with the presence of blanching defects ($P < 0.05$) in univariate analysis were further analyzed using multivariate analysis with binary logistic regression. All models were adjusted for age, sex, injected dose, and BMI, in addition to the interactions between correlated variables (e.g., arm position and tracer group), as appropriate.

Agreement between the 2 primary readers on the total count of blanching defects per participant was compared using the intraclass correlation coefficient. Agreement on the qualitative evaluation (i.e., the presence or absence of blanching defects, laterality, and grade) was compared using Cohen κ-analysis.

RESULTS

Study Participants

The general characteristics of the study population are given in Table 1. Group 1 (^{18}F-FDG) included 18 women and 29 men with a mean age of 51.2 ± 13.2 y (range, 26.0–78.0 y). Compared with group 1, group 2 participants were all men ($P < 0.001$), older (71.0 ± 8.3 vs. 51.2 ± 13.3 y, $P < 0.001$), taller (178.1 ± 7.8 vs. 171.8 ± 9.8 cm, $P = 0.002$), and marginally heavier (91.0 ± 16.7 vs. 83.5 ± 16.9 kg, $P = 0.06$); however, their mean BMI was comparable to group 1. The groups had comparable setups regarding

TABLE 1
General Characteristics of Study Participants

Characteristic	^{18}F-FDG dose (n = 47)			Fluciclovine (standard dose)
	Low	Intermediate	Standard	
Age (y)	45 ± 11.1 (26–62)	51.7 ± 9.3 (39–66)	55.1 ± 15 (26–78)	71.0 ± 8.3 (54.1–89)
Weight (kg)	78.4 ± 16.1 (53.1–102.5)	95 ± 17.9 (77–131.7)	81.8 ± 15.1 (53–113)	91.0 ± 16.7 (68.4–148)
Height (cm)	173.6 ± 10.5 (157.5–195.6)	170.6 ± 12.4 (152.4–193)	171.1 ± 8.3 (157.5–185.4)	178.1 ± 7.8 (165.1–195.6)
BMI (kg/m^2)	25.8 ± 3.4 (20.4–32.2)	32.6 ± 4.5 (26.8–40.4)	28 ± 5.3 (19.4–37)	28.7 ± 5.4 (19.4–46.8)
Injected dose (MBq)	19.6 ± 1.7 (17.2–23.5)	188.4 ± 8.6 (175.7–196.7)	372.3 ± 17.0 (331.9–393.8)	314.6 ± 19.7 (287.2–389.6)
Fasting duration (h)	9.2 ± 3.0 (6–15)	11.4 ± 3.4 (6–18)	11 ± 2.9 (6–20)	6.9 ± 3.4 (4–16)
Blood glucose (mg/dL)	90.7 ± 19.2 (39–113)	94.3 ± 12.7 (76–113)	97.9 ± 21.8 (65–154)	Not applicable
Sex				
Female	7	2	9	0
Male	8	8	13	30
Disease				
Cancer	0	0	7	30
Cardiovascular	0	10	0	0
Healthy	15	0	15	0
Imaging time points				
Dynamic and delayed	15	10	15	0
Dynamic only	0	0	7	30
Arms position				
Above head	0	0	0	29
To sides	15	10	22	1
Attenuation-corrected CT dose				
Ultralow (5 mAs)	15	10	15	0
Low (50 mAs)	0	0	7	30
PET/CT misregistration				
No	10	8	17	25
Yes	5	2	5	5

Qualitative data are number; continuous data are mean and range.

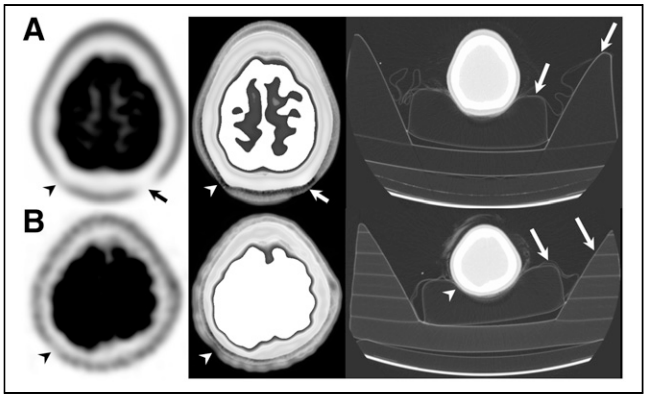

FIGURE 1. Example of complete (A) and partial (B) blanching defects. (A) Images from 29-y-old healthy woman weighing 81 kg and 165 cm tall, injected with ^{18}F-FDG (369 MBq). PET image (left) demonstrates bilateral posterior parietooccipital scalp defects, complete on left side (arrow) and partial on right side (arrowhead). ^{18}F-FDG PET/CT image (middle) shows no CT abnormality. Lung window (right) outlines head support setup (arrows). (B) Images from 43-y-old healthy woman weighing 53 kg and 160 cm tall, injected with ^{18}F-FDG (18.5 MBq). PET image (left) demonstrates relative photopenia at right posterior parietal scalp region (arrowhead), representing partial blanching defect. Contralateral side (left side) shows no abnormality. ^{18}F-FDG PET/CT image (middle) shows no CT abnormality at site of partial defect. Lung window (right) outlines head position within support setup (arrows) and demonstrates minimal tilting of skull toward side of partial defect (arrowhead). Color version of this figure is available as supplemental file at http://tech.snmjournals.org.

the positioning aids (namely, the use of knee and back cushions). A head support was used for all participants.

Of the 77 participants, 37 had cancer (30 prostate and 7 with urothelial tumors) and 10 had cardiovascular disease (with a history of recent myocardial infarction), whereas the remaining 30 were healthy participants not known to have had a recent myocardial infarction or cancer.

Agreement Analysis

There was no significant difference in the number of reported blanching defects per participant between the 2 readers (2.5 ± 1.8 vs. 2.6 ± 1.6, $P = 0.5$), with an intraclass correlation coefficient of 0.90 (95% CI, 0.85–0.94). Also, there was moderate to substantial agreement (range, 0.66–0.88) on reporting of the blanching defect laterality and grade, both on a participant basis and on a site basis (Table 2).

Characteristics of Blanching Defects

All encountered blanching defects from both groups were seen in both attenuation-corrected and non–attenuation-corrected images. On the final reading, 124 blanching defects in total were seen in 68 of 77 (88%) participants at one or more pressure points.

The average number of defects was higher in group 2 (3.5 ± 1.7) than in group 1 (2.1 ± 1.4; $P < 0.001$) but did not vary within group 1 for different ^{18}F-FDG dose subgroups. On average, 2.2 ± 1.3, 2.0 ± 1.6, and 2.1 ± 1.5 defects were observed per participant in the low-, intermediate-, and standard-dose groups, respectively ($P = 0.8$).

TABLE 2
κ-Agreement on Defect Detection/Laterality and Grade between 2 Readers According to Scan Time Point and Evaluated Pressure Points

Scan timing and evaluated pressure points	Agreement	
	Detection*	Grade of defect
Dynamic only	0.81 (0.75–0.88)	0.81 (0.75–0.83)
90-min only	0.66 (0.44–0.88)	0.70 (0.49–0.91)
Skull	0.76 (0.62–0.89)	0.75 (0.60–0.89)
Scapulae	0.84 (0.74–0.95)	0.88 (0.80–0.95)
Sacrum	0.72 (0.55–0.89)	0.74 (0.60–0.89)
Calcaneus	0.78 (0.66–0.90)	0.82 (0.73–0.92)

*Agreement figures on detection also include agreement on laterality.

Data in parentheses are 95% CI.

Blanching defects against the scapulae and calcaneus on dynamic imaging were the most frequent and tended to be bilateral and complete (Table 3). Only 14 partial defects from 9 participants were still seen on the delayed static images (90 min after injection) (Fig. 2). No complete blanching defects were seen on the 90-min images. The distribution of the blanching defects is summarized in Table 3. Among the 7 participants who had follow-up dynamic scanning, 6 defects were encountered at baseline compared with 8 in the follow-up scans. The distribution, laterality, and grade changed between the 2 scans within the same participant. For example, one participant who previously showed bilateral complete defects opposite the calcaneus demonstrated only a unilateral partial calcaneal defect on the repeated scan (Fig. 3).

Blanching defects beyond the above-described pressure points were not systematically evaluated; however, we noticed variable degrees of blanching defects at other sites where bony parts press against a tightened or hard structure: for example, prominent spinous processes at the cervicodorsal region at the site of transition between the head support and the scanner table; elbows against the scanning table or immobilization belts; distal parts of the legs against the end of knee cushions when the heels are not touching the scanning table; and the forefeet against the tightened immobilization aids (Fig. 4).

Factors Associated with Presence of Blanching Defects

On a participant basis, the presence or absence of blanching defects on dynamic scans did not vary according to age, sex, height, weight, BMI, injected dose, fasting hours, or blood glucose level. Also, the use of cushions (back or knee) and misregistration between the PET and CT were not associated with these defects. Twenty-nine of 30 participants in group 2 had their arms up and showed one or more defects, compared with 39 of 47 with arms to the side ($P = 0.01$).

TABLE 3
Distribution of Blanching Defects According to Anatomic Site, Laterality, and Grade on Dynamic and Delayed Imaging

	Dynamic (n = 77)				Delayed static (n = 40)*			
Blanching defect	Skull	Scapulae	Sacrum	Calcaneus	Skull	Scapulae	Sacrum	Calcaneus
Absent	53	43	58	9	37	37	38	32
Present	24	34	19	47	3	3	2	6
One or unilateral								
Partial	8	2	8	1	1	2	2	3
Complete	5	3	11	7	0	0	0	0
Two or bilateral								
Partial	3	8	NA	4	2	1	NA	3
Complete†	8	21	NA	35	0	0	NA	0
Outside field of view	0	0	0	21	0	0	0	2

*37 of original 77 participants did not undergo 90-min imaging.
†In presence of bilateral defects with different defect grades, higher grade was recorded for that pressure point.
NA = not applicable because sacrum was evaluated as single pressure point.

On a site basis (Supplemental Table 1; supplemental materials are available at http://jnmt.snmjournals.org), the clinical and scan features associated with the presence of blanching defects varied according to the anatomic site. On univariate analysis, both skull and scapular defects were seen more frequently in group 2 participants (older participants who were scanned with their arms up). Furthermore, scapular defects were encountered significantly more often in taller men. However, in multivariate analysis, only arm positioning above the head was associated with skull defects (odds ratio, 11.5; 95% CI: 3.7–35.7; $P < 0.001$) whereas scapular and sacral defects were associated with a lower BMI and the male sex. Defects around the calcaneus were not associated with any of the studied characteristics.

The use of back or knee cushions did not significantly affect the frequency or distribution of these defects. However, back pillows were used in only 4 participants. Knee cushions, on the other hand, were used for most participants; nevertheless, they were not associated with the presence of defects opposite the calcaneus.

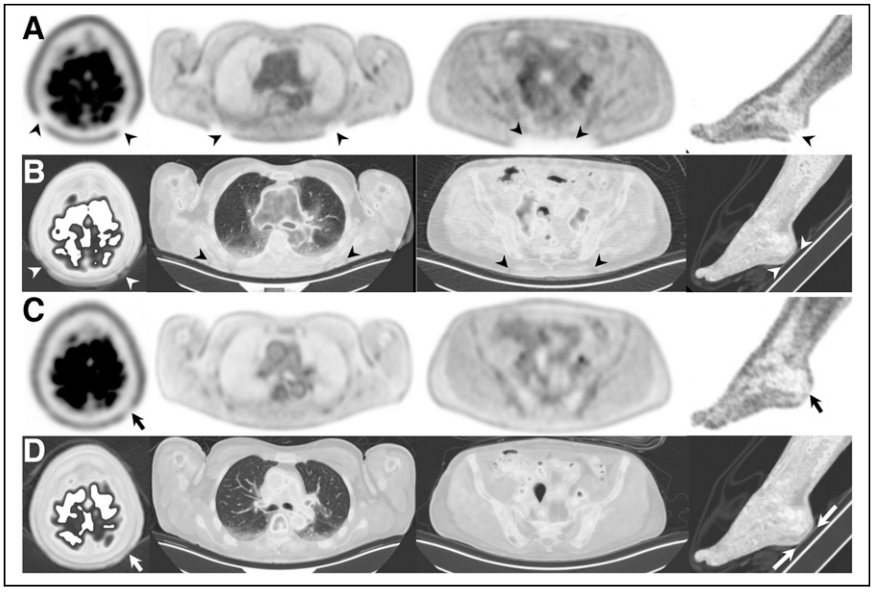

FIGURE 2. Examples of partial and complete restoration of uptake within complete blanching defects seen at pressure points, from left to right, against skull and scapulae bilaterally, sacrum, and left calcaneus. (A–D) PET images from last 20 min of dynamic 60-min acquisition (A), their respective 20-min static acquisition at 90 min (C), and corresponding PET/CT images (B and D) in lung window, to demonstrate relationship with positioning setup and scanner table. Sites with complete defects on dynamic images are marked with arrowheads, and sites with partial restoration at 90-min time point are marked with arrows. Blanching defects against skull showed complete restoration on right side and partial restoration on left side, and those against scapulae and sacrum showed complete restoration, whereas defects opposite heel showed partial restoration on delayed 90-min image. Color version of this figure is available as supplemental file at http://tech.snmjournals.org.

DISCUSSION

In this study, we found that dynamic total-body PET/CT imaging frequently demonstrated multiple areas of absent or markedly diminished radiotracer uptake against pressure points. These areas included the sides of the scalp, being pressed against the parietal bones, and the skin and subcutaneous tissues opposite the bony prominences of the scapulae, sacrum, and calcaneus.

We hypothesize that these defects may be related to the absence of decreased perfusion induced by mechanical compression, or displacement of the

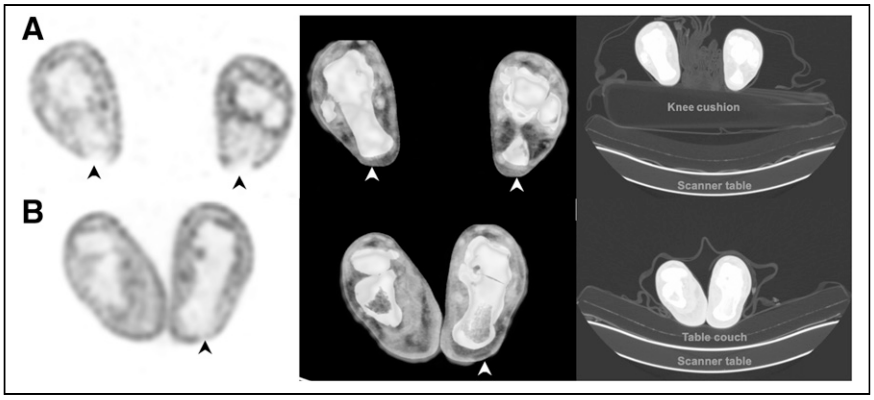

FIGURE 3. Changes in pattern of blanching defects against calcaneus in same subject across 2 dynamic scans, baseline (A) and follow-up (B), separated by 2 wk. Shown are representative images from 74-y-old man with genitourinary cancer weighing 74 kg and 170 cm tall. ^{18}F-FDG PET images demonstrate bilateral complete blanching defects opposite calcaneus (A, arrowheads), with no corresponding abnormality in PET/CT image (middle). Follow-up dynamic PET scan in same subject shows unilateral partial defect on left foot (B, arrowhead). CT images with lung window (right) outline positioning setup demonstrating relationship of heels with respect to knee cushion (top) and table couch (bottom) during respective scan time points. Color version of this figure is available as supplemental file at http://tech.snmjournals.org.

blood within the microcirculation at the pressure sites near the bony prominence, where the skin and subcutaneous tissue are known to be thinned and the pressure is high (*18*). This hypothesis is supported by several findings: that the defects followed a close anatomic distribution and photopenic patterns regardless of the uptake mechanism of the tracer, that the defects improved or resolved on delayed imaging when the participants were allowed to walk freely and return to the same scanning position, and that the defects lacked anatomic correlations at these sites on the CT images (e.g., skin discontinuity, ulceration, or necrotic masses). Though dynamic PET acquisitions have been well established, especially for brain imaging, the current observation has not previously been described, to our knowledge. One possible explanation, at least partially, is the outstanding gain in scanner sensitivity, which makes subtle observations far more obvious than with conventional scanners.

Although most PET/CT imaging centers use simplified static approaches in the clinical setting, dynamic acquisition protocols are increasingly included in guidelines (*13–17*). Therefore, identification and characterization of these blanching defects may have both clinical and research relevance, particularly for the interpretation of routine ^{18}F-fluciclovine scans. ^{18}F-fluciclovine PET/CT imaging guidelines (*16*) recommend early scanning around 3–5 min after injection (with the dynamic acquisition protocol being optional). Accordingly, most institutions inject the tracer while the patient is lying on the scanner table and then begin the PET data acquisition either immediately or around 4 min after injection, starting at the pelvis and moving cranially. This protocol is acquired primarily with the arms above the head. This position leads to scapular rotation upward and may also increase tension on the posterior paraspinal cervical muscles, thereby adding pressure on the skull. In our data, the scalp and scapular defects were encountered more frequently in group 2 participants.

In our work, 40 participants underwent delayed static imaging 30 min after the end of a 60-min dynamic PET acquisition. In 31 of them, the uptake was normalized at the pressure points. We assume that resumption of tracer delivery and uptake after prolonged cessation of circulation at these pressure points may be partially explained by a mechanism similar to the tourniquet effect (*19*), in which prolonged pressure may cause a temporary local decrease in perfusion and subsequent compensatory vasodilation after release of the pressure, redelivering part of the circulating tracer in the blood pool to the sites with defects. Only 9 participants continued to demonstrate partial defects at one or more pressure points (Table 3). We hypothesize that the magnitude of pressure (in terms of force and duration) may be related to the rate of resumption of the circulation at these points and may vary under different physiologic and pathologic conditions. This hypothesis may be clinically relevant for assessment of cutaneous microvascular circulation. Currently, the capillary refill-time test is commonly used as a simple means to assess macrovascular disease and cutaneous perfusion (*20*). In this test, the examiner applies firm external pressure by a finger to the distal phalanx of a finger or toe, and the time required to recover the normal skin color is recorded. The test, though simple and widely used, is not standardized regarding the magnitude or duration of the applied pressure, the cutoff for abnormality, or the interpretation criteria. Also, it lacks sensitivity and reliability, with wide inter- and intraobserver variability (*21*). Accordingly, many other methods for assessing peripheral perfusion have been introduced (*22*). The highly sensitive total-body PET scanners can capture and quantify radiotracer dynamic processes as they occur in real time, simultaneously with other organ and tissue kinetics (*7,8,23*), and may be used to study different mechanopathologic conditions such as pressure ulcers. These possibilities warrant further exploration in a prospective setting.

Finally, we note some limitations of the current study. Although the data were prospectively collected in the context of other projects, this study was based on retrospective serendipitous evaluation of these scans, and accordingly, potential clinical characteristics and additional tests that might relate to the current findings were not collected. For example, scapular and sacral defects were encountered

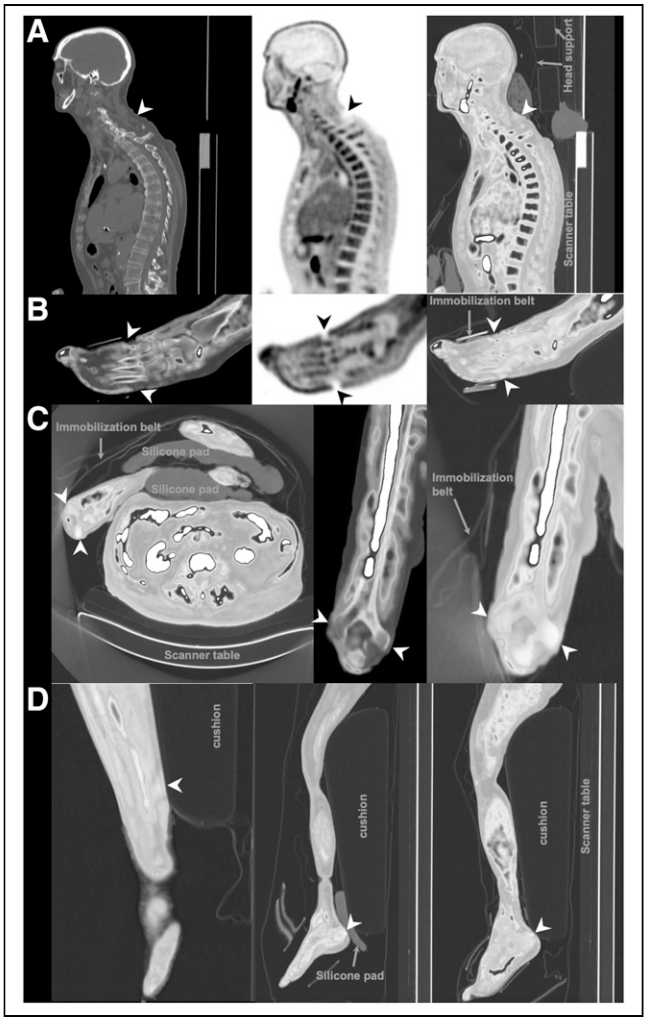

FIGURE 4. Examples of other nonsystematic blanching defects (arrowheads). (A) Absence of skin and subcutaneous ^{18}F-fluciclovine uptake opposite cervicodorsal vertebrae at site of transition between head support and scanner table, as might be caused by pressure against prominent spinous processes. (B) Absence of ^{18}F-FDG uptake at dorsum of foot at site of tightened immobilization belt. (C) Reduced-to-absent ^{18}F-fluciclovine uptake opposite medial and lateral epicondyles of right humerus at site of wrapped immobilization belt around elbows. (D) A few additional patterns of blanching defects in lower limb: at distal third of calf as it is pressing against end of knee cushion (left), opposite calcaneus although silicon pad was placed to minimize pressure (middle), and again opposite calcaneus at end of knee/leg cushion, where heels do not touch scanner table (right). Color version of this figure is available as supplemental file at http://tech.snmjournals.org.

more frequently in men with a lower BMI, potentially indicating that sex differences, hormonal status, and fat volume could contribute to the finding. Also, local skin conditions that could have been appreciated with direct inspection, the Raynaud phenomenon, or autoimmune diseases were not captured in this report. The microcirculation is tightly controlled under numerous external and internal pathophysiologic mechanisms, and the current work cannot provide further direct clinical implications of the described findings. Also, because the study was retrospective, we could not demonstrate a clear association with the positioning setup of the participants—a setup that could be far more complex than mere descriptions of body build, cushion location, type, geometry, or any other characteristics of positioning aids. Additionally, we limited our results to 7 pressure points, whereas in realty a few other blanching defects could be encountered (Fig. 4). The sporadic nature of these defects prevents accurate systematic evaluation. Furthermore, the position of the arms was tightly linked to the tracer group. Although we compensated for the interaction term between these 2 variables, we believe that a homogenous distribution of arms up and arms down in each tracer group would be preferable. Another limitation was the relatively high frequency of misregistration between the PET and CT components of the images. In a total-body scanner, the whole body is covered within the field of view during the whole acquisition duration; accordingly, any motion in one region of the body could affect the attenuation correction and scatter correction in other regions (*2*). With the high sensitivity of total-body PET, data-driven motion compensation techniques could be explored as a potential solution (*24*).

CONCLUSION

Blanching defects opposite pressure points are common on dynamic total-body PET/CT imaging using the uEXPLORER scanner with different radiopharmaceuticals and injection doses. Their appearance should not be immediately interpreted as an abnormality. The changes in tracer distribution taking place at the pressure points across the body can be captured in real time on the high-sensitivity total-body PET/CT scanner and can be leveraged in a prospective setting to study various circulatory changes occurring in different mechanopathologic conditions such as pressure ulcers.

DISCLOSURE

The University of California, Davis, has a research- and revenue-sharing agreement with United Imaging Healthcare. Ramsey Badawi, Simon Cherry, Guobao Wang, and Lorenzo Nardo are investigators on a research grant funded by United Imaging Healthcare. This work is supported in part by NIH R01 CA249422, NIH R01CA206187, NIH R35 CA197608, NIH UL1TR001860, NIH T32HL086350, and a CTSC pilot grant. No other potential conflict of interest relevant to this article was reported.

ACKNOWLEDGMENTS

We thank Denise T. Caudle, Ofilio Vigil, Lynda Painting, and Dana Little from the University of California, Davis, for their support.

KEY POINTS

QUESTION: Are there any unusual findings opposite the pressure points on dynamic total-body PET imaging?

PERTINENT FINDINGS: Blanching defects, described as areas with markedly decreased or completely absent radiotracer uptake in the skin or subcutaneous tissue at the pressure points opposite the skull, scapulae, sacrum, and calcaneus, were seen in 39 of 47 (^{18}F-FDG) and 29 of 30 (^{18}F-fluciclovine) total-body dynamic scans.

IMPLICATIONS FOR PATIENT CARE: Blanching defects are commonly encountered on dynamic total-body PET imaging with both ^{18}F-FDG or ^{18}F-fluciclovine and should not be mistaken for any abnormality.

REFERENCES

1. Nardo L, Abdelhafez YG, Spencer BA, Badawi RD. Clinical implementation of total-body PET/CT at University of California, Davis. *PET Clin.* 2021;16:1–7.
2. Ng QK, Triumbari EKA, Omidvari N, Cherry SR, Badawi RD, Nardo L. Total-body PET/CT: first clinical experiences and future perspectives. *Semin Nucl Med.* 2022;52:330–339.
3. Spencer BA, Berg E, Schmall JP, et al. Performance evaluation of the uEXPLORER total-body PET/CT scanner based on NEMA NU 2-2018 with additional tests to characterize PET scanners with a long axial field of view. *J Nucl Med.* 2021;62:861–870.
4. Badawi RD, Shi H, Hu P, et al. First human imaging studies with the EXPLORER total-body PET scanner. *J Nucl Med.* 2019;60:299–303.
5. Wang G, Nardo L, Parikh M, et al. Total-body PET multiparametric imaging of cancer using a voxelwise strategy of compartmental modeling. *J Nucl Med.* 2022; 63:1274–1281.
6. Liu G, Hu P, Yu H, et al. Ultra-low-activity total-body dynamic PET imaging allows equal performance to full-activity PET imaging for investigating kinetic metrics of ^{18}F-FDG in healthy volunteers. *Eur J Nucl Med Mol Imaging.* 2021;48: 2373–2383.
7. Wu Y, Feng T, Zhao Y, et al. Whole-body parametric imaging of ^{18}F-FDG PET using uEXPLORER with reduced scanning time. *J Nucl Med.* 2022;63:622–628.
8. Feng T, Zhao Y, Shi H, et al. Total-body quantitative parametric imaging of early kinetics of ^{18}F-FDG. *J Nucl Med.* 2021;62:738–744.
9. Sarkar S, Matsukuma KE, Spencer B, et al. Dynamic positron emission tomography/computed tomography imaging correlate of nonalcoholic steatohepatitis. *Clin Gastroenterol Hepatol.* 2021;19:2441–2443.
10. Turkbey B, Mena E, Shih J, et al. Localized prostate cancer detection with ^{18}F FACBC PET/CT: comparison with MR imaging and histopathologic analysis. *Radiology.* 2014;270:849–856.
11. Tulipan AJ, Vlatkovic L, Malinen E, et al. Comparison of time curves from dynamic ^{18}F-fluciclovine positron emission tomography and dynamic contrast-enhanced magnetic resonance imaging for primary prostate carcinomas. *Phys Imaging Radiat Oncol.* 2018;7:51–57.
12. Uprimny C, Kroiss AS, Decristoforo C, et al. Early dynamic imaging in ^{68}Ga-PSMA-11 PET/CT allows discrimination of urinary bladder activity and prostate cancer lesions. *Eur J Nucl Med Mol Imaging.* 2017;44:765–775.
13. Morbelli S, Esposito G, Arbizu J, et al. EANM practice guideline/SNMMI procedure standard for dopaminergic imaging in Parkinsonian syndromes 1.0. *Eur J Nucl Med Mol Imaging.* 2020;47:1885–1912.
14. Law I, Albert NL, Arbizu J, et al. Joint EANM/EANO/RANO practice guidelines/SNMMI procedure standards for imaging of gliomas using PET with radiolabelled amino acids and [^{18}F]FDG: version 1.0. *Eur J Nucl Med Mol Imaging.* 2019;46: 540–557.
15. Sciagrà R, Lubberink M, Hyafil F, et al. EANM procedural guidelines for PET/CT quantitative myocardial perfusion imaging. *Eur J Nucl Med Mol Imaging.* 2021;48: 1040–1069.
16. Nanni C, Zanoni L, Bach-Gansmo T, et al. [^{18}F]fluciclovine PET/CT: joint EANM and SNMMI procedure guideline for prostate cancer imaging—version 1.0. *Eur J Nucl Med Mol Imaging.* 2020;47:579–591.
17. Varrone A, Asenbaum S, Vander Borght T, et al. EANM procedure guidelines for PET brain imaging using [^{18}F]FDG, version 2. *Eur J Nucl Med Mol Imaging.* 2009;36:2103–2110.
18. Cichowitz A, Pan WR, Ashton M. The heel: anatomy, blood supply, and the pathophysiology of pressure ulcers. *Ann Plast Surg.* 2009;62:423–429.
19. Desaia A, Intenzo C. The "tourniquet effect." *J Nucl Med.* 1984;25:697–699.
20. Fleming S, Gill P, Jones C, et al. The diagnostic value of capillary refill time for detecting serious illness in children: a systematic review and meta-analysis. *PLoS One.* 2015;10:e0138155.
21. Pickard A, Karlen W, Ansermino JM. Capillary refill time: is it still a useful clinical sign? *Anesth Analg.* 2011;113:120–123.
22. Liu C, Correia R, Ballaji H, Korposh S, Hayes-Gill B, Morgan S. Optical fibre sensor for simultaneous measurement of capillary refill time and contact pressure. *Sensors (Basel).* 2020;20:1388.
23. Qi J, Matej S, Wang G, Zhang X. 3D/4D reconstruction and quantitative total body imaging. *PET Clin.* 2021;16:41–54.
24. Berg E, Revilla EM, Abdelhafez YG, et al. Framework design for comprehensive patient motion compensation in total-body PET. EventClass website. https://www.eventclass.org/contxt_ieee2020/online-program/session?s=M-10. Accessed August 11, 2022.